Modeling the Effect of Finite-Rate Hydrogen Diffusion on Porosity Formation in Aluminum Alloys

KENT D. CARLSON, ZHIPING LIN, and CHRISTOPH BECKERMANN

A volume-averaged model for finite-rate diffusion of hydrogen in the melt is developed to predict pore formation during the solidification of aluminum alloys. The calculation of the micro-/macro-scale gas species transport in the melt is coupled with a model for the feeding flow and pressure field. The rate of pore growth is shown to be proportional to the local level of gas supersaturation in the melt, as well as various microstructural parameters. Parametric studies of one-dimensional solidification under an imposed temperature gradient and cooling rate illustrate that the model captures important phenomena observed in porosity formation in aluminum alloys. The transition from gas to shrinkage dominated porosity and the effects of different solubilities of hydrogen in the eutectic solid, capillary pressures at pore nucleation, and pore number densities are investigated in detail. Comparisons between predicted porosity percentages and previous experimental measurements show good correspondence, although some uncertainties remain regarding the extent of impingement of solid on the pores.

DOI: 10.1007/s11663-006-9013-2

I. INTRODUCTION

POROSITY-RELATED defects are a major cause of casting rejection and rework in the casting industry. They are typically caused by a lack of feeding of the shrinkage that occurs during solidification or by excessive levels of gas species dissolved in the melt. Modeling of porosity formation has been attempted by many researchers, dating back to the early one-dimensional (1-D) work of Piwonka and Flemings[1] and the seminal two-dimensional (2-D) work of Kubo and Pehlke.[2] An extensive review of the research progress in porosity modeling, from these early studies up to the work done in 2000, is provided by Lee *et al.*[3] Recent examples of porosity models for aluminum alloy castings, including the effect of dissolved hydrogen, can be found in Sabau and Viswanathan[4] and Pequet *et al.*[5] These models assume that the local diffusion of hydrogen in the melt is infinitely fast. In a series of experimental and theoretical studies, Lee and co-workers[6–10] have shown that diffusion of hydrogen through the supersaturated liquid (inside the mushy zone) to the pores can be a rate-controlling factor in pore growth for aluminum alloys. Lee and Hunt[6,7] experimentally observed porosity formation in aluminum alloys using an X-ray temperature gradient stage. They found the pressure drop caused by shrinkage to be negligibly small. They developed a microscale model of hydrogen diffusion-controlled growth by considering a single pore inside the mushy zone. The model does not compute the pressure field in the mushy zone; rather, the pressure is an input variable. Atwood *et al.*[8,9] applied this model to an Al7Si alloy, and Hamilton *et al.*[10] incorporated it into a heat flow model for complex-shaped castings, still neglecting pressure variations. Hence, a comprehensive porosity model that simultaneously accounts for hydrogen diffusion and shrinkage is still lacking.

Figure 1 shows porosity percentages resulting from directional solidification experiments performed by several researchers using unmodified aluminum alloy A356.[11–14] Note that in every study, covering a range of initial hydrogen concentrations C_0, the pore volume decreases as the cooling rate during solidification increases. If the porosity was the result of a lack of feeding flow (*i.e.*, shrinkage-related porosity), then the trend in this figure would be the opposite; the pore volume would increase with solidification cooling rate. This can be understood by considering the Niyama criterion.[16] The Niyama criterion, which is based on the liquid pressure drop across the mushy zone, is a local thermal parameter given by the ratio $G/\sqrt{\dot{T}}$, where G is the temperature gradient and $\dot{T}$ is the cooling rate. Based on its derivation, the Niyama criterion applies to shrinkage porosity only, and not to gas porosity (note that the dissolved gas content is not even a parameter in the Niyama criterion). Shrinkage porosity generally increases as the Niyama criterion value decreases (*e.g.*, with increasing cooling rate).[17] This is the opposite of the trend seen in Figure 1, indicating that the porosity seen in this figure is not shrinkage related. It should be

KENT D. CARLSON, Research Engineer, ZHIPING LIN, Graduate Research Assistant, CHRISTOPH BECKERMANN, Professor, are with the Department of Mechanical and Industrial Engineering, The University of Iowa, Iowa City, IA 52242. Contact e-mail: becker@engineering.uiowa.edu.

This article is based on a presentation made in the symposium "Simulation of Aluminium Shape Casting Processing: From Design to Mechnacial Properties" which occured March 12–16, 2006, during the TMS Spring meeting in San Antonio, Texas, under the auspices of the Computational Materials Science and Engineering Committee, the Process Modelling, Analysis and Control Committee, the Solidification Committee, the Mechanical Behavior of Materials Committee, and the Light Metal Division/Aluminium Committee.

Article published online February 27, 2007.

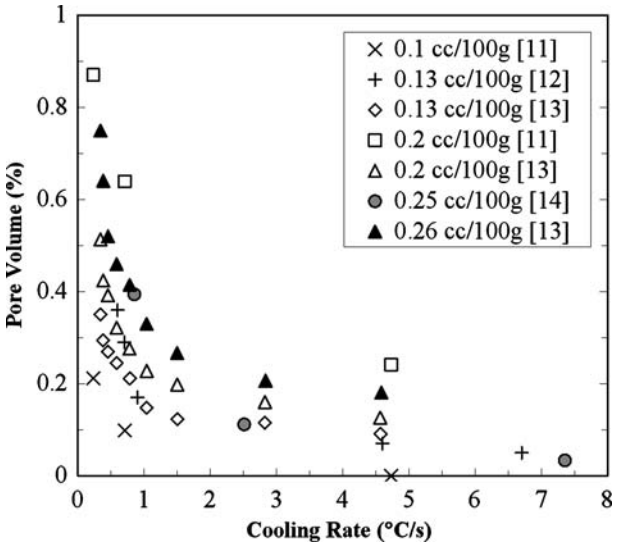

Fig. 1—Porosity percentages as a function of cooling rate for various initial hydrogen concentrations (given in $cc_{STP}H_2/100$ g Al) in unmodified A356, from directional solidification experiments.[11–14] All results are pore volume percentages except for those of Reference 11, which are pore area percentages. However, if the area percentage is a representative sample, the area percentage is equal to the volume percentage.[15]

noted that the temperature gradient, G, was not held constant in the experiments corresponding to Figure 1, which could cause variations in the Niyama criterion value in addition to those due to cooling rate; however, it is shown subsequently that the temperature gradients in these experiments are well above the values that would cause shrinkage porosity. If the porosity is then gas related, one is still left searching for an explanation as to why gas porosity decreases so notably with increasing cooling rate. One possible physical mechanism is that pore formation in these experiments is indeed controlled by diffusion of hydrogen in the melt toward the pores, as originally proposed by Lee and co-workers.[6–10] If that is the case, then an increasing cooling rate would reduce the porosity, because less time is available during solidification for the gas species to diffuse toward the pores. The current work will explore this issue in detail.

The present study of porosity formation in aluminum alloys focuses on incorporating into the porosity model of Carlson *et al.*,[18] a model for local, finite-rate gas species diffusion through the liquid metal to the pores. Unlike the finite-rate diffusion work of Lee and co-workers,[6–10] which modeled hydrogen diffusion to a single pore, the present approach uses a volume-averaging approach, which is easily incorporated into an existing macroscale model for porosity formation and feeding flow during casting solidification.[18] As in Reference 18, the pressure field and feeding flows in the liquid metal as well as in the mushy zone are determined using a single-domain approach. Because pressure and feeding flow calculations are included, this study models both shrinkage-related and gas-related porosity, including the effects of finite-rate gas diffusion. The model is tested for 1-D, directional solidification of the (unmodified) alloy A356. The results are compared to measurements available in the literature. The importance of accounting for finite-rate diffusion of hydrogen to the pores is demonstrated.

II. MODEL DESCRIPTION

The present multiphase model assumes that an averaging volume (Figure 2(a)) is composed of some combination of solid metal (s), liquid metal (l), and porosity (p), such that the volume fractions satisfy $\varepsilon_s + \varepsilon_l + \varepsilon_p = 1$. Mixture properties are given by the sum of the property values for each phase multiplied by their respective volume fractions. For example, the mixture density is given by $\rho = \varepsilon_s\rho_s + \varepsilon_l\rho_l + \varepsilon_p\rho_p$. For the purpose of the parametric studies presented subsequently, the temperature field is prescribed.

The mixture continuity equation is simplified by assuming that the solid metal and the porosity are stationary. The continuity equation is then given by[18]

$$\frac{\partial}{\partial t}\left(\varepsilon_s\rho_s + \varepsilon_l\rho_l + \varepsilon_p\rho_p\right) + \nabla\cdot(\rho_l\mathbf{v}) = 0 \qquad [1]$$

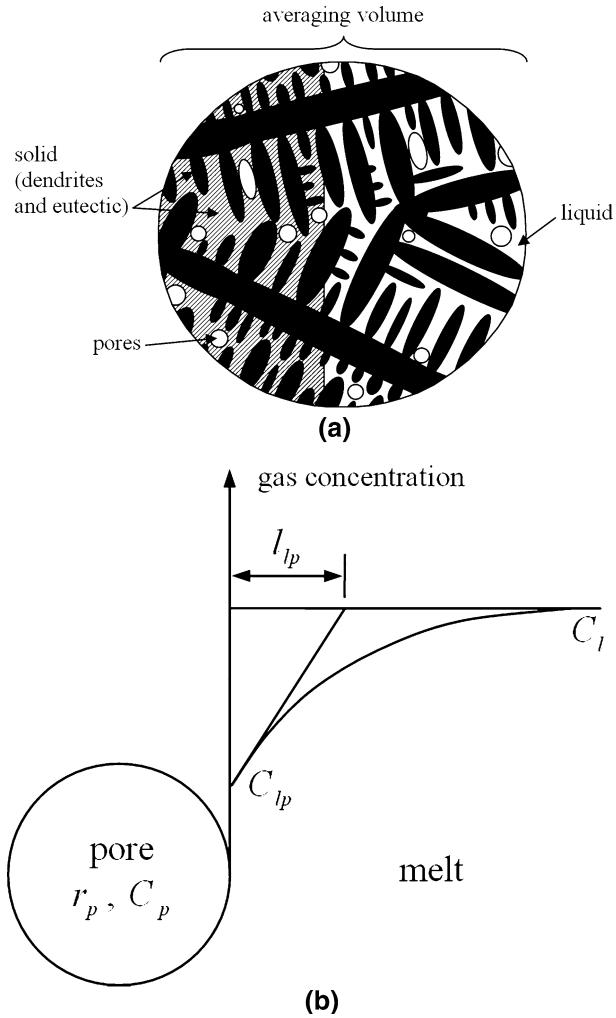

Fig. 2—Schematics showing (*a*) a typical averaging volume and (*b*) a hydrogen diffusion boundary layer around a growing pore.

or

$$\nabla \cdot \mathbf{v} = -\frac{1}{\rho_l}\left[\frac{\partial}{\partial t}\left[\varepsilon_s(\rho_s - \rho_l) + \rho_l - \varepsilon_p(\rho_l - \rho_p)\right] + \mathbf{v} \cdot \nabla \rho_l\right] \quad [2]$$

where $\mathbf{v}$ denotes the superficial liquid velocity, $\mathbf{v} = \varepsilon_l \mathbf{v}_l$. Equation [2] shows that the divergence of the velocity field is a function of the solidification contraction, liquid density change, porosity evolution, and gradients in the liquid density (although this last contribution is small).

The volume-averaged liquid momentum equation is given by[18]

$$\nabla^2 \mathbf{v} = \frac{\varepsilon_l}{K}\mathbf{v} + \frac{\varepsilon_l}{\mu_l}\nabla P - \frac{\varepsilon_l}{\mu_l}\rho_{ref}\mathbf{g} \quad [3]$$

where P is the melt pressure; $\mathbf{g}$ is the gravity vector; ρ_{ref} is a reference liquid density, taken as the melt density at the liquidus temperature; and μ_l is the dynamic viscosity of the liquid. Buoyancy-induced flow and inertial terms are neglected. The permeability, K, is assumed to be given by $K = K_0 \varepsilon_l^3/(1-\varepsilon_l)^2$, where $K_0 = \lambda_2^2/180$, in which λ_2 is the secondary dendrite arm spacing (SDAS). The SDAS is determined from $\lambda_2 = \left[\lambda_{2,0}^3 + M(t - t_L)\right]^{1/3}$, where $\lambda_{2,0}$ is an initial spacing, M is a coarsening constant, and $(t\text{-}t_L)$ is the time (in seconds) elapsed since solidification began. The values chosen for $\lambda_{2,0}$ and M in the present study are provided in Table I. The values were selected to obtain agreement with SDAS models and experimental data provided for A356 in the literature.[19,20] Notice that Eq. [3] reduces to Stokes' equation in the single-phase liquid region, where K becomes very large. In the mushy zone, the left-hand side of Eq. [3] becomes very small relative to the permeability term, and the equation then reduces to Darcy's law.

By manipulating and combining Eqs. [2] and [3], it is possible[18] to derive the following equation for the melt pressure, P:

$$\nabla \cdot \left(\frac{K}{\mu_l}\nabla P\right) = -(\nabla \cdot \mathbf{v}) + \nabla \cdot \left(\frac{K}{\mu_l}\rho_{\text{ref}}\mathbf{g}\right) + \nabla \cdot \left(\frac{K}{\varepsilon_l}\nabla^2 \mathbf{v}\right) \quad [4]$$

where $(\nabla \cdot \mathbf{v})$ is given by the right-hand side of Eq. [2].

The average concentration of hydrogen dissolved in the melt, C_l (in wt fraction), is obtained from the mixture gas species conservation equation:[18]

$$\frac{\partial}{\partial t}\left(\varepsilon_s \rho_s C_s + \varepsilon_l \rho_l C_l + \varepsilon_p \rho_p C_p\right) + \nabla \cdot (\rho_l C_l \mathbf{v}) = 0 \quad [5]$$

The concentration of hydrogen in the solid (assuming fast diffusion) is approximately given by $C_s = \kappa_{sl} C_l$, where κ_{sl} is the partition coefficient of hydrogen between the solid and liquid. In the present study, κ_{sl} was calculated using the liquid and solid solubilities of hydrogen in A356, as described in Section III. Because the porosity is assumed to be composed of hydrogen only, the hydrogen concentration in the pores is unity (*i.e.*, $C_p = 1$).

As stated in Section I, the growth of pores is modeled in the present study by considering local (microscale) diffusion of the gas species toward the pores, which are characterized by a uniform gas species concentration, C_p. As illustrated in Figure 2(b), the gas species concentration in the melt is not uniform. At the pore-liquid interface, the concentration in the melt is equal to the equilibrium value C_{lp}, which is given by Sievert's law as a function of the pore pressure and temperature (as subsequently discussed). Away from the pores, the gas species concentration increases toward the average concentration in the melt, C_l. It is this gradient in the gas species concentration in the melt that drives pore growth. Following the same volume averaging principles as in Ni and Beckermann,[25] a gas species conservation equation for the pore phase can be written as

$$\frac{\partial}{\partial t}\left(\varepsilon_p \rho_p C_p\right) = C_{lp}\frac{\partial}{\partial t}\left(\varepsilon_p \rho_p\right) + \frac{S_{lp}\rho_l D_l}{l_{lp}}\left(C_l - C_{lp}\right) \quad [6]$$

Table I. Properties and Parameters Used for A356 Simulations (Unless Otherwise Noted); When Temperature T Appears in the Table, the Units are Absolute Temperature (K)

Parameter (Units)	Value	Reference
Initial SDAS value, λ_2^0 (μm)	15	19, 20
Coarsening factor, M (μm^3/s)	870	19, 20
Initial pore radius, r_0 (μm)	1	—
Surface tension, σ (N/m)	0.8	21
Hydrogen gas constant, R (J/kg K)	4124	22
Hydrogen diffusion coefficient, D_l (m^2/s)	$D_l = 3.8 \times 10^{-6} \exp\left(-\frac{2315}{T}\right)$	23
Equilibrium coefficient, K_e (wt pct)	$\log_{10} K_e = -\frac{2691.96}{T} - 1.32$	24
First-order Si interaction parameter, e_{H}^{Si} (wt pct^{-1})	$e_{\text{H}}^{\text{Si}} = \exp\left(\frac{417}{T} - 4.38\right)$	24
First-order Cu parameter, e_{H}^{Cu} (wt pct^{-1})	$e_{\text{H}}^{\text{Cu}} = \exp\left(\frac{1485}{T} - 4.92\right)$	24
First-order Mg parameter, e_{H}^{Mg} (wt pct^{-1})	$e_{\text{H}}^{\text{Mg}} = -0.066$	24
First-order Fe parameter, e_{H}^{Fe} (wt pct^{-1})	$e_{\text{H}}^{\text{Fe}} = \exp\left(\frac{5299}{T} - 8.17\right)$	24
First-order Zn parameter, e_{H}^{Zn} (wt pct^{-1})	$e_{\text{H}}^{\text{Zn}} = \exp\left(-\frac{954}{T} - 3.14\right)$	24
First-order Ti parameter, e_{H}^{Ti} (wt pct^{-1})	$e_{\text{H}}^{\text{Ti}} = -1.80 \times 10^{-4} T + 0.155$	24
Second-order Si interaction parameter, r_{H}^{Si} (wt pct^{-2})	$r_{\text{H}}^{\text{Si}} = -1.00 \times 10^{-6} T + 5.23 \times 10^{-4}$	24
Second-order Cu parameter, r_{H}^{Cu} (wt pct^{-2})	$r_{\text{H}}^{\text{Cu}} = 1.40 \times 10^{-6} T - 2.01 \times 10^{-3}$	24
All other second-order parameters (wt pct^{-2})	$r_{\text{H}}^{\text{Mg}} = r_{\text{H}}^{\text{Fe}} = r_{\text{H}}^{\text{Zn}} = r_{\text{H}}^{\text{Ti}} = 0$	24

where S_{lp} is the area of the interface between the liquid and the pores per unit volume, D_l is the gas species mass diffusion coefficient in the liquid, and l_{lp} is the gas species diffusion length in the liquid at the pore-liquid interface. In writing Eq. [6], it is assumed that the pore-solid interface is stationary and that gas species diffusion through the solid toward the pores is negligible. The two terms on the right-hand side of Eq. [6] account, respectively, for the movement of the pore-liquid interface and the diffusion of the gas species through the liquid toward the pores. Solving Eq. [6] for the rate of increase of the pore mass per unit volume yields

$$\frac{\partial}{\partial t}\left(\varepsilon_p \rho_p\right) = \frac{S_{lp}\rho_l D_l}{l_{lp}} \frac{\left(C_l - C_{lp}\right)}{C_p - C_{lp}} + \frac{\varepsilon_p \rho_p}{C_p - C_{lp}} \frac{\partial C_p}{\partial t} \quad [7]$$

For a single gas species (*i.e.*, hydrogen), $C_p = 1$, and Eq. [7] can be simplified to

$$\frac{\partial}{\partial t}\left(\varepsilon_p \rho_p\right) = \frac{S_{lp}\rho_l D_l}{l_{lp}} \frac{\left(C_l - C_{lp}\right)}{1 - C_{lp}} = \gamma_{lp}\Omega_l \quad [8]$$

The second equality in Eq. [8] defines a pore growth factor $\gamma_{lp} = S_{lp}\rho_l D_l / l_{lp}$ and a normalized liquid supersaturation $\Omega_l = (C_l - C_{lp})/(1 - C_{lp})$. The diffusion length is calculated from $l_{lp} = r_p$, where r_p is the average pore radius in an averaging volume; this expression is based on the well-known analytical result for the quasi-steady species boundary layer thickness around a sphere (Figure 2(b)). It can easily be shown that for typical pore growth rates encountered during solidification, unsteady effects on gas species diffusion in the melt are negligibly small. The pore-liquid interfacial area concentration is approximated as $S_{lp} = 4\pi n r_p^2 \phi$, where n is the number density of pores and ϕ is an impingement factor, taken as $\phi = (1 - \varepsilon_s)^m$. The impingement factor accounts for the fact that, during solidification, an increasing fraction of the pore interfacial area is "covered" by solid, rather than by liquid. Figure 3 shows how the impingement factor varies as a function of solid fraction for different values of m; larger values of m reduce the impingement factor for a given solid fraction. An investigation of the effect of m on the porosity predictions can be found in Section IV.

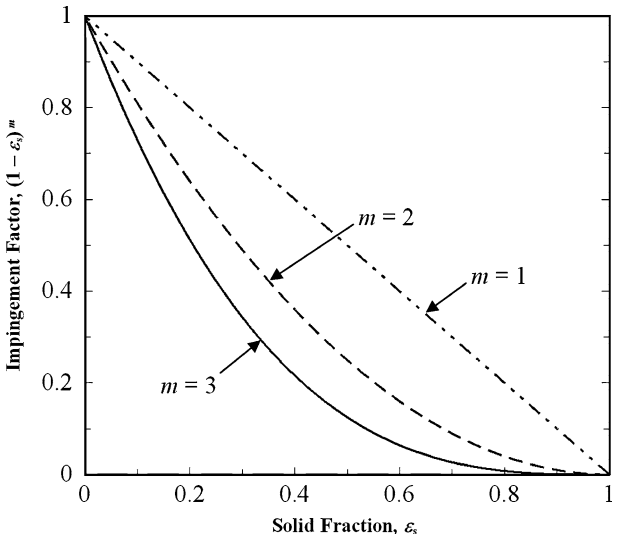

Fig. 3—Variation of impingement factor with solid fraction, for three different impingement factor exponents.

Equation [8] shows that for a finite supersaturation in the melt, when the average gas species concentration in the liquid, C_l, is larger than the equilibrium concentration at the liquid-pore interface, C_{lp}, hydrogen diffuses toward the pore and the pore grows (*i.e.*, ε_p increases). For large γ_{lp}, which occurs for a large interfacial area (*e.g.*, with a high pore density, n) or for a small diffusion length, the melt becomes well mixed (C_l tends to C_{lp}), because the pore growth rate $\partial(\varepsilon_p \rho_p)/\partial t$ must be finite. Note from Eq. [8] that the pore volume fraction, ε_p, also changes in response to changes in the pore density, ρ_p. The pore density is calculated from the ideal gas law, $\rho_p = P_p/(\mathrm{R}T)$, where P_p is the pore pressure, R is the gas constant for hydrogen, and T is the absolute temperature. In the present model, Eq. [8] is actually solved for the equilibrium concentration at the liquid-pore interface, C_{lp}. As in Reference 18, the pore volume fraction, ε_p, is then determined from the continuity equation, Eq. [1]. Hence, the effects of feeding flow, solidification shrinkage, and other density changes on ε_p are still taken into account.

The pore pressure is calculated from Sievert's law:

$$\frac{P_p}{P_{\mathrm{atm}}} = \left[\frac{C_{lp}}{(K_e/f)}\right]^2 \quad [9]$$

When no pores are present, C_l is used in place of C_{lp}. In Eq. [9], K_e and f are the equilibrium and activity coefficients of the hydrogen gas species, respectively. The ratio K_e/f represents the solubility of hydrogen in the liquid phase at atmospheric pressure, C_l^*. The determination of the equilibrium and activity coefficients is described in Section III. Note that Eq. [9] neglects the effect of interface curvature on C_{lp}.

Porosity is assumed to nucleate if $P \le P_p - P_\sigma$, where P_σ is the capillary pressure. When porosity forms, the melt pressure at that location is forced to $P = P_p - P_\sigma$.[18] The capillary pressure is modeled as

$$P_\sigma = \frac{2\sigma}{\max\left(r_p; r_{\mathrm{nuc}}\right)} \quad [10]$$

where σ is the surface tension of the pore-liquid interface. The effective pore radius at nucleation, r_{nuc}, may be calculated from $r_{\mathrm{nuc}} = r_0/\Phi$, where r_0 is the initial pore radius and Φ is a heterogeneous nucleation parameter (less than unity). However, neither the initial pore radius nor the heterogeneous nucleation parameter is known to any degree of accuracy. More importantly, pores do not typically nucleate in the melt; rather, they evolve from tiny gas pockets on entrained oxide films or other inclusions. Therefore, r_{nuc} is simply used in the present study as a parameter to control the maximum capillary pressure, $P_{\sigma,\mathrm{nuc}} = 2\sigma/r_{\mathrm{nuc}}$, at which the pores begin to grow

"freely." In the following, the initiation of free pore growth is still referred to as nucleation. The effect of $P_{\sigma,\mathrm{nuc}}$ on the porosity predictions is investigated in a parametric study in Section IV. Once $r_p > r_{\mathrm{nuc}}$, Eq. [10] gives the capillary pressure corresponding to a pore with a radius of curvature equal to r_p.

Finally, the average pore radius is calculated as in Pequet *et al.*[5] from

$$r_p = \max\left[r_0; \min\left(r_{\mathrm{sphere}}; r_{\mathrm{dend}}\right)\right] \qquad [11]$$

where $r_{\mathrm{sphere}} = [3\varepsilon_p/(4\pi n)]^{1/3}$ and $r_{\mathrm{dend}} = \lambda_2(1-\varepsilon_s)/(2\varepsilon_s)$. In the equation for r_{dend}, ε_s is held constant once the eutectic starts to form, because the eutectic grows between rather than on the secondary dendrite arms. Also, r_{dend} is held constant once $r_p = r_{\mathrm{dend}}$, because the pores cannot displace solid and the solid cannot grow into the pores. Once the pore radius is equal to r_{dend}, the pores continue to grow between the dendrite arms by assuming an ellipsoidal shape. When the length of the (ellipsoidal) pores exceeds the distance between the pores ($\approx n^{-1/3}$), the pores begin to merge, creating so-called "connected" porosity. It can be seen in the model for the pore radius, as well as in the model for the pore interfacial area concentration, that the pore number density, n, plays an important role. Because the size distribution of pore initiation sites is generally not known, it is difficult to develop a quantitative model for the evolution of the pore number density. Therefore, n must remain an input parameter for the purpose of the present study. The effect of different pore number densities on the porosity predictions is investigated in detail in Section III.

III. MATERIAL PROPERTIES

The present study was performed for the aluminum alloy A356, with the composition listed in Table II. This particular composition was selected to closely match compositions reported for the experiments that are used in the present study to validate the model predictions.[13,14] The solidification path and other casting-relevant material properties (density, viscosity, and weight percent of alloying elements in the liquid metal during solidification) were determined using the aluminum module of the thermodynamic simulation software package JMatPro.[26] The simulation was performed using a Scheil analysis and allowing all phases available in the database to form. The solidification cutoff was specified to be 0.1 pct. As discussed subsequently, this value gives close agreement between the measured and predicted temperatures at which the alloy is completely solidified.

Table II. Composition of the A356 Alloy Modeled in the Present Study

Element	Amount (Wt Pct)
Si	7.0
Mg	0.37
Fe	0.10
Ti	0.08
Zn	0.01
Cu	0.01
Mn	0.01
Al	balance

The resulting material data are presented as a function of temperature in Figure 4. The solidification path is shown in Figure 4(a), including solid fraction curves for each phase that forms during solidification. The liquidus and 100 pct solid (termed "solidus," for simplicity) temperatures resulting from this simulation were T_{liq} = 616 °C and T_{sol} = 551 °C, respectively. The pronounced kink in the total solid fraction curve that occurs at 574 °C is due to the initial formation of the eutectic (Si) phase. The smaller jump in the solidification path that occurs at 557 °C, and increases the total solid fraction to near unity, corresponds to the formation of the Mg_2Si phase. This phase can more readily be seen in the inset in Figure 4(a), which also indicates that small amounts of two other phases form in the latter stages of solidification. These temperatures (and the corresponding solid fractions) for liquidus, solidus, eutectic formation, and Mg_2Si formation are in good agreement with measured values for unmodified A356 found in the literature.[27] Several different densities are plotted in Figure 4(b) along with the solid fraction (the thick line), which is shown for reference. The various rises and drops in the liquid density and solid density curves are caused by the formation of phases that begin to transform heavier or lighter elements from liquid to solid. The solid density shown in Figure 4(b) is given by $\rho_s = \sum_k f_{s,k} / \sum_k \left(f_{s,k}/\rho_{s,k}\right)$, where k represents each solid phase, and $f_{s,k}$ and $\rho_{s,k}$ are the mass fraction and density of that solid phase, respectively. The dashed line in Figure 4(b) is the mixture density, which is given by $\rho = 1/(f_s/\rho_s + f_l/\rho_l) = \varepsilon_s\rho_s + \varepsilon_l\rho_l$, where $f_s = \sum_k f_{s,k}$ is the total solid mass fraction; note that the final equality is the same as that given in Section II for the mixture density, assuming no porosity is present. The weight percent of each alloying element in the liquid is shown in Figure 4(c). Again, the solid fraction is also shown for reference, as a thick line. As solidification proceeds, the silicon content in the liquid increases from 7 to about 13 wt pct. Also, note that the amount of magnesium in the liquid rises substantially after the eutectic phase begins to form; this continues until Mg_2Si forms late in solidification. Finally, the dynamic viscosity is shown in Figure 4(d). The viscosity increases steadily as the temperature decreases.

Other properties necessary for the present simulations are the solubility of hydrogen in the liquid phase at atmospheric pressure, C_l^*, and the hydrogen partition coefficient, κ_{sl}. As mentioned in conjunction with Eq. [9], C_l^* is given by $C_l^* = K_e/f$. The equilibrium coefficient, K_e, which indicates the solubility of hydrogen in pure aluminum, is given as a function of temperature by $\log_{10}K_e = -a/T - b$, where a and b are constants (Table I) and T is the absolute temperature. The activity coefficient, f, is calculated as a function of the alloying element concentrations in the melt by $\log_{10} f = \sum_X \left[e_H^X C_l^X + r_H^X \left(C_l^X\right)^2\right]$, where X is an alloying

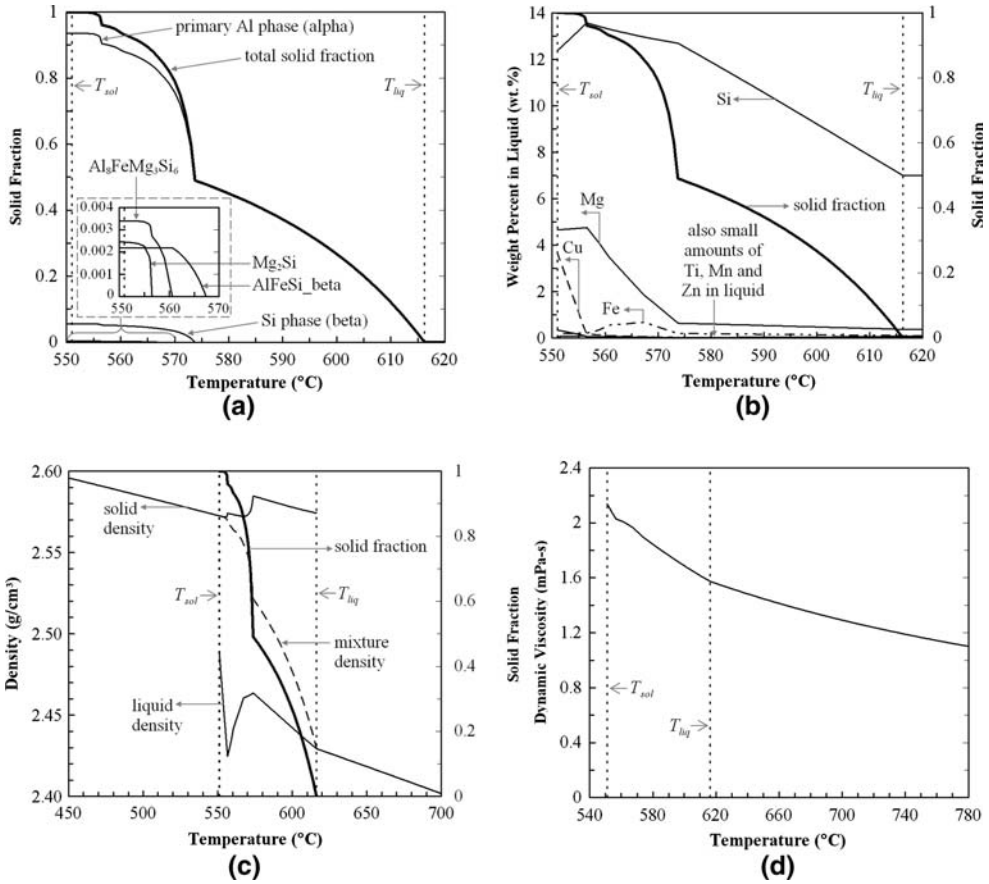

Fig. 4—A356 property values as a function of temperature: (*a*) solid fractions of each phase that forms; (*b*) liquid phase, solid phase and mixture densities; (*c*) weight percent of each alloying element in the liquid; and (*d*) dynamic viscosity of the liquid.

element in an Al-H-X solution (X = Cu, Si, Mg, Zn, Fe, or Ti), C_l^X are the concentrations (in wt pct) of the alloying elements in the melt (Figure 4(c)), and e_H^X and r_H^X are interaction parameters (Table I). The values of a, b, e_H^X, and r_H^X used in this study are from the data of Anyalebechi.[24] Anyalebechi determined the equilibrium coefficient values a and b from a combined linear regression analysis of nine different sets of reliable experimental data. The relations provided in Table I for e_H^X and r_H^X were determined using Anyalebechi's data for these parameters at 973 and 1023 K; data were also provided at 1073 and 1123 K, but only the two data sets nearest the liquidus temperature were used to develop the equations given in Table I. It is assumed that these data can be extrapolated down through the solidification range. The liquid solubility, C_l^*, is shown in the upper right portion of Figure 5(a).

The partition coefficient, κ_{sl}, is assumed to be given by $\kappa_{sl} = C_s^*/C_l^*$, where C_s^* is the solubility of hydrogen in the solid.[28] The present model for the solid solubility, C_s^*, is based on the work of Poirier and Sung.[28] They developed a model for hydrogen solubility in aluminum-silicon alloys using the experimental data of Ichimura and Sasajima[29] for Al-Si alloys with Si contents ranging from 2 to 14 pct. The model of Poirier and Sung has the form $C_s^* = \left[\left(K_{e,\alpha}/f_H^\alpha\right)f_\alpha + K_{e,\beta}f_\beta\right]/\left(f_\alpha + f_\beta\right)$, where $K_{e,\alpha}$ and $K_{e,\beta}$ (both in weight percent) are the equilibrium coefficients of hydrogen in the solid alpha (*i.e.*, primary aluminum) and solid beta (*i.e.*, silicon) phases; f_H^α represents the activity coefficient of hydrogen resulting from the silicon in the primary aluminum phase; and f_α and f_β are the solid mass fractions of the alpha and beta phases, respectively. Note that for a completely solidified Al-Si alloy, $f_\alpha + f_\beta = 1$. Poirier and Sung used the data of Anyalebechi[30] for $K_{e,\alpha}$, resulting in the expression $\ln K_{e,\alpha} = -6830.2/T - 5.1725$. Accounting also for the temperature dependence of $K_{e,\beta}$ and f_H^α, the solid solubility equation of Poirier and Sung can be rewritten as follows:

$$C_s^* = \left(\exp\left\{\frac{-6830.2}{T} - 5.1725 - \left[\frac{a_1}{T} + b_1\right]C_\alpha^{Si}\right\}f_\alpha + \exp\left[\frac{a_2}{T} + b_2\right]f_\beta\right)\Big/\left(f_\alpha + f_\beta\right) \quad [12]$$

where C_α^{Si} is the amount of silicon in the alpha phase (in wt pct), and T is the absolute temperature. Using the experimental data of Ichimura and Sasajima,[29] Poirier and Sung employed an optimization routine to find the best values of a_1, b_1, a_2, and b_2. While their predictions with Eq. [12] agree reasonably well with the data in Reference 29, the solubility predicted by Eq. [12] behaves rather strangely: in the solidifying and solid metal, the solubility increases as the temperature decreases. Because this seems physically unrealistic, a

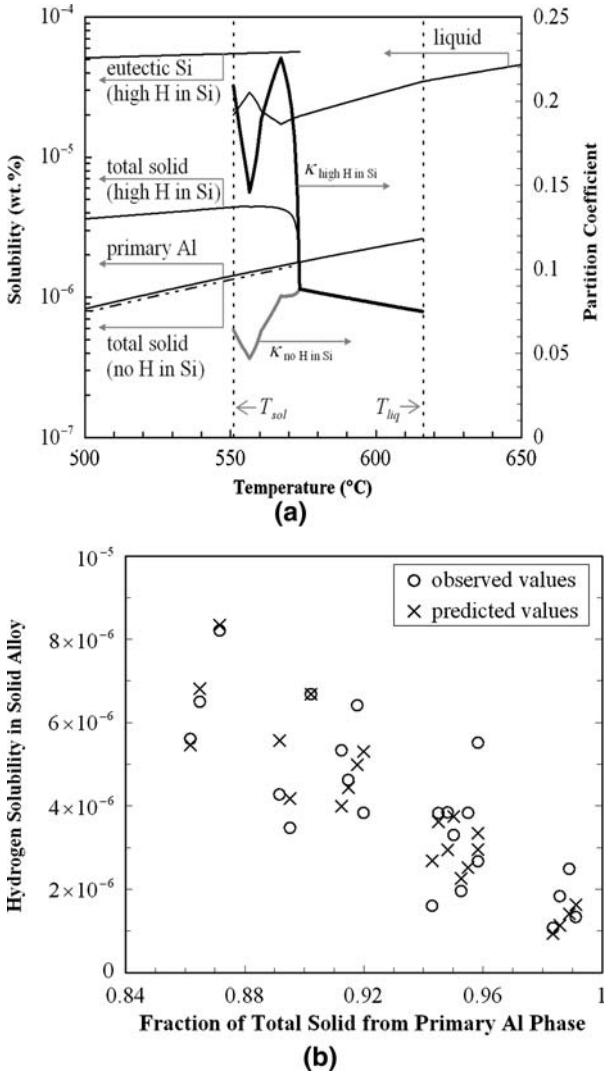

Fig. 5—Aluminum alloy solubility data: (*a*) liquid and solid solubilities and partition coefficient as a function of temperature for A356; and (*b*) predicted and observed[29] solubilities of hydrogen in solid aluminum-silicon alloys.

modification of this model was used in the present study. Rather than trying to optimize four coefficients with the data from Reference 29, it was decided to reduce the number to two by assuming an activity coefficient f_{H}^{α} of unity; this assumption may be justified by the fact that the mass fraction of silicon in the primary aluminum phase is small. This gives a solid solubility expression of the form

$$C_s^* = \left[\exp\left(\frac{-6830.2}{T} - 5.1725\right) f_\alpha + \exp\left(\frac{a_3}{T} + b_3\right) f_\beta\right] \Big/ \left(f_\alpha + f_\beta\right) \qquad [13]$$

A mathematical package was used to perform a regression analysis to find the best fit of Eq. [13] to the data of Ichimura and Sasajima,[29] as presented by Poirier and Sung.[28] This resulted in the coefficients $a_3 = -877.4$ and $b_3 = -8.747$. A comparison between the experimental solubilities of Ichimura and Sasajima and the predictions given by Eq. [13] is shown in Figure 5(b). The agreement between predicted and observed values is reasonable and similar to that obtained by Poirier and Sung. However, the solubility now decreases with decreasing temperature in the solid, as anticipated. The expression given in Eq. [13] is plotted in Figure 5(a) and labeled as the solubility of hydrogen in the total solid, with high hydrogen content in the eutectic silicon (*i.e.*, "total solid (high H in Si)"). It should be mentioned that the mass fractions of the higher order (> 2) phases in the A356 alloy (inset in Figure 4(a)), which account for less than 1 pct of the total mass, were simply combined with the primary aluminum fraction, f_α. Note the increase in the solubility, C_s^*, when the eutectic phase begins to form. This is explained subsequently.

Although hydrogen is known to have a very low solubility in solid silicon (~10^{-15} to 10^{-11} wt pct in the temperature range of interest[31]), Ichimura and Sasajima[29] found that hydrogen solid solubilities in Al-Si alloys tended to increase with increasing silicon content. This can be seen from Figure 5(b), by noting that hydrogen solubility increases with decreasing primary aluminum phase fraction (which corresponds to increasing silicon content) in solidified Al-Si alloys. Using the coefficients a_3 and b_3 determined previously, the solubility of hydrogen in the silicon phase is given by $\ln C_s^* = -877.4/T - 8.747$, which is of the order of 10^{-5} wt pct (see the curve in the upper left of Figure 5(a), labeled "eutectic Si (high H in Si)"). One possible explanation to reconcile this difference in the solubilities of hydrogen in silicon is that hydrogen becomes "trapped" at the interfaces between the primary and eutectic phases of Al-Si alloys, thus giving the appearance of a higher solubility in the silicon than is generally accepted to be reasonable.[28]

On the other hand, if it is assumed that the solubility of hydrogen in the eutectic Si is, in fact, negligibly small, then Eq. [13] reduces to

$$C_s^* = \left[\exp\left(\frac{-6830.2}{T} - 5.1725\right) f_\alpha\right] \Big/ \left(f_\alpha + f_\beta\right) \qquad [14]$$

This equation is plotted in Figure 5(a) and labeled "total solid (no H in Si)." For comparison, this curve is shown along with the curve for the solubility of hydrogen in the primary aluminum phase, $K_{e,\alpha}$. There is very little difference in these two curves, which is to be expected because there is less than 6 wt pct eutectic Si in the final solidified alloy.

Finally, Figure 5(a) shows two different partition coefficients, $\kappa_{sl} = C_s^*/C_l^*$, as a function of temperature. One corresponds to the coefficient determined using C_s^* from Eq. [13] (labeled "$\kappa_{\text{high H in Si}}$"), and the other corresponds to the coefficient determined using C_s^* from Eq. [14] (labeled "$\kappa_{\text{no H in Si}}$"). When the high value of hydrogen solubility in the eutectic Si is used, the partition coefficient increases to an average value of about 0.19 after the eutectic forms. When hydrogen

solubility in the eutectic Si is considered negligible, however, the partition coefficient drops to an average of about 0.07 after the eutectic forms. The effect of these differences in the partition coefficient on the porosity predictions is investigated in Section IV.

IV. RESULTS

Numerical simulations were conducted for the directional solidification system illustrated in Figure 6. The system domain is 1-D (in x), with a zero-flow boundary condition at the left ($x = 0$) side and atmospheric pressure applied at the right (inflow) boundary. A linear temperature profile is translated across the domain with a constant speed given by $\dot{T}/G$, where $\dot{T}$ and G are the cooling rate and temperature gradient, respectively. In the parametric studies presented subsequently, $\dot{T}$ and G are specified independently of each other. Unless otherwise noted, the simulations use the partition coefficient corresponding to very low solubility of hydrogen in the silicon phase, $\kappa_{\text{no H in Si}}$.

In order to closely approximate the thermal conditions in the experiments that are employed later in this section to validate the porosity predictions,[13,14] the following expression is used to relate the temperature gradient (in °C/m) to the cooling rate (in °C/s): $G = 3265\dot{T}^{0.512}$. This expression was developed by simulating the directional solidification experiments in References 13 and 14. Both of these experiments created nearly 1-D solidification conditions by using a refractory mold and employing a high cooling rate, created using water spray cooling, on one end of the casting. These experiments were both simulated using the casting simulation software *MAGMASOFT*.[32] The heat-transfer coefficient at the end of the casting where the water spray cooling was applied was adjusted until the simulated cooling rates agreed with the reported cooling rates measured at various points in the experimental castings. Simulated cooling rates were calculated using the cooling rate definitions specified in each experiment: Reference 13 reported cooling rates as average values between 570 °C and 620 °C, while Reference 14 used the average values between solidus and liquidus, which were about 542 °C and 613 °C, respectively. Once the simulated cooling rates agreed with the experimental values, the temperature gradients and cooling rates were again evaluated at the same locations in the simulation as previously used, but rather than using average values over a temperature range, they were evaluated at the eutectic temperature and at the solidus temperature. It is believed that for the purpose of the present porosity predictions, the temperature gradients and cooling rates between the eutectic and solidus temperatures are more representative of the conditions during porosity formation than the values near the liquidus temperature. The resulting temperature gradient *vs* cooling rate plot is given in Figure 7. This figure shows data from the simulations of both experiments, with values evaluated at both the eutectic and solidus temperatures. Finally, a power-law regression line was fitted to all the data shown in Figure 7, which led to the temperature gradient expression listed previously.

Figure 8 shows profiles of some of the calculated dependent variables for an initial hydrogen level in the melt of $C_0 = 0$, a cooling rate of $\dot{T} = 0.1$ ° C/s, and a temperature gradient of $G = 1000$ °C/m. In this simulation, the growth factor, γ_{lp}, is set to a very large value, thereby modeling complete (infinitely fast) local diffusion of hydrogen in the melt. The pore density is taken as 10^{11} pores/m^3, and the maximum capillary pressure, $P_{\sigma,\text{nuc}} = 2\sigma/r_{\text{nuc}}$, as 1.6 bar, which corresponds to $r_{\text{nuc}} \approx 10$ μm. The temperature increases linearly in the positive x direction, as shown in Figure 6. Results are shown at a time in the simulation when there is a fully solidified layer next to $x = 0$. Figure 8(a) indicates that for zero initial hydrogen content, the melt pressure drops significantly at the end of solidification, due to the

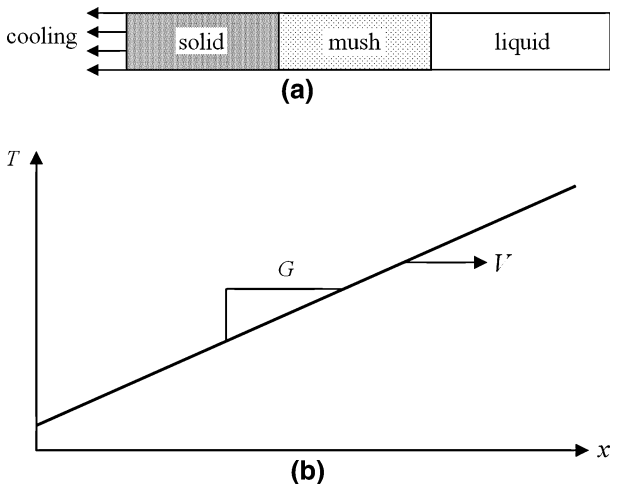

Fig. 6—(*a*) Schematic of one-dimensional solidification, brought about by cooling one end of the 1-D domain. (*b*) The prescribed temperature profile characterized by the temperature gradient, G, and the solidification front velocity, V.

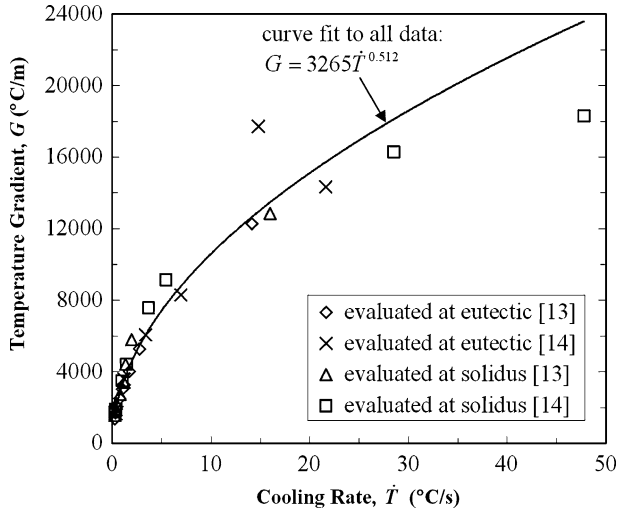

Fig. 7—Curve fit relating the temperature gradient to the cooling rate. Data points shown are from simulations of experiments performed by Emadi and Gruzleski[13] and Fang and Granger[14].

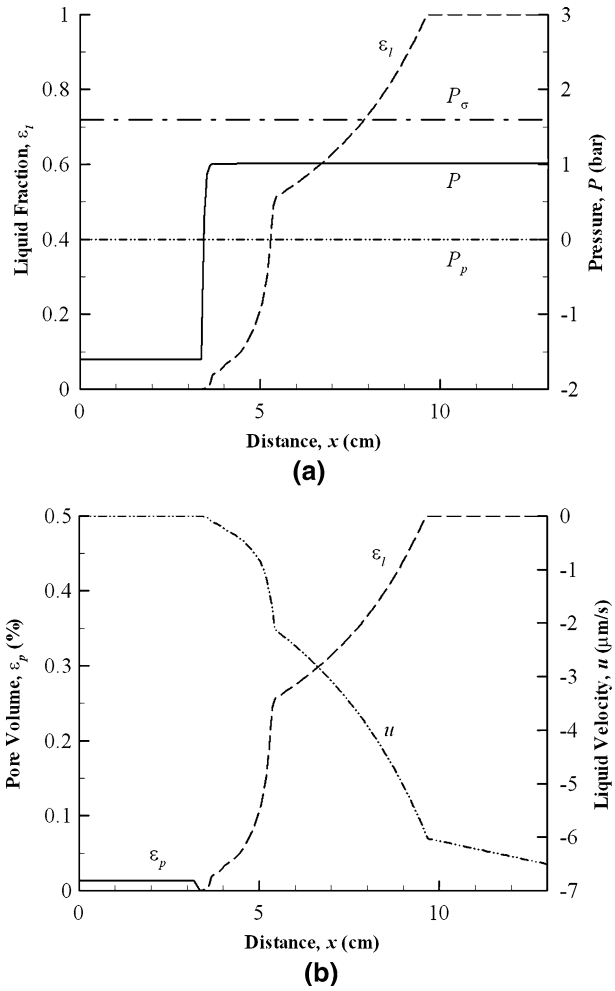

Fig. 8—1-D simulation results as a function of distance with an initial hydrogen concentration of $C_0 = 0$: (*a*) the relevant pressures and (*b*) the velocity and pore volume percentage. This simulation uses an infinite hydrogen diffusion rate, $\dot{T} = 0.1$°C/s, $G = 1000$ °C/m, $n = 10^{11}$ m^{-3}, and a capillary pressure at a nucleation of 1.6 bar.

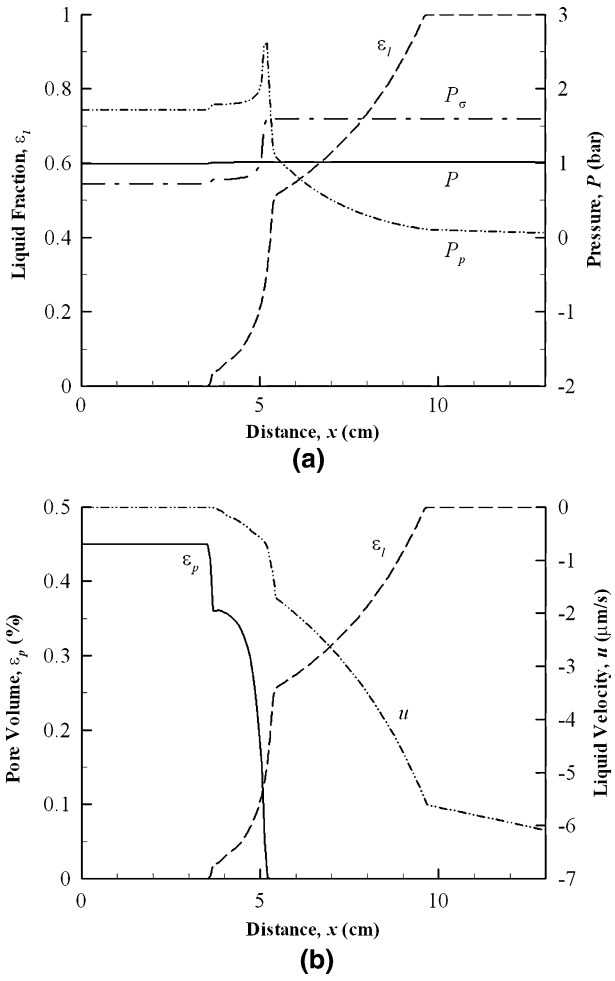

Fig. 9—1-D simulation results as a function of distance with an initial hydrogen concentration of $C_0 = 0.13$ cc/100 g: (*a*) the relevant pressures and (*b*) the velocity and pore volume percentage. This simulation uses an infinite hydrogen diffusion rate, $\dot{T} = 0.1$°C/s, $G = 1000$ °C/m, $n = 10^{11}$ m^{-3}, and a capillary pressure at nucleation of 1.6 bar.

sharp decrease in the permeability, as the liquid fraction approaches zero. Because there is no hydrogen in this simulation, the pore pressure is zero everywhere. The melt pressure rapidly decreases until the pore formation condition is satisfied (*i.e.*, $P_p = 0 \geq P + P_\sigma$), after which the melt pressure is simply $P = -P_\sigma$. When the pore formation condition is met, porosity forms, as seen in Figure 8(b). The amount of porosity grows until solidification is complete, but the final value is small because pore formation begins very late in solidification. This figure also shows the velocity distribution. Note that the velocity is always negative, indicating that the feeding flow is always moving in the negative x direction (*i.e.*, toward the solidifying metal), as expected.

Figure 9 shows analogous profiles for a simulation run with the same conditions as in Figure 8, except that the initial hydrogen content is $C_0 = 0.13$ $cc_{STP}H_2/100$ g Al. In contrast with Figure 8, Figure 9 indicates that porosity in this case does not form due to a significant melt pressure drop (very little melt pressure drop occurs here), but rather due to a significant increase in the pore pressure, P_p. The pore pressure profile before pore formation illustrates the increase in the equilibrium gas pressure with decreasing temperature, according to Sievert's law. When the pore pressure becomes large enough to meet the pore formation condition (shortly after the beginning of the eutectic reaction, when the liquid fraction, ε_l, is about 50 pct), porosity begins to form. The porosity grows until the melt is completely solidified. Note that the capillary pressure, P_σ, rapidly reduces from the initial value of $P_{\sigma,\text{nuc}} = 1.6$ bar to about 0.8 bar, due to the increase in the pore radius, r_p, during the initial pore growth stage; subsequently, P_σ remains constant at 0.8 bar, because r_p is limited by the dendritic network (r_{dend}). Once porosity forms, the pore pressure merely reflects changes in the melt and capillary pressures (because $P_p = P + P_\sigma$). The velocity profile in Figure 9(b) is similar to that in Figure 8(b), but the magnitude is a little smaller. This is because less feeding flow is required in the latter simulation, because more porosity has formed to feed the shrinkage.

Before exploring the effect of finite-rate diffusion of hydrogen in the liquid in more detail, it is important to better understand the role of the maximum capillary

pressure at the beginning of pore growth, $P_{\sigma,\text{nuc}}$, on porosity formation. Thus, a number of simulations were performed with an infinitely fast hydrogen diffusion rate (*i.e.*, $\gamma_{lp} \to \infty$). The results, shown in Figure 10, correspond to $\dot{T} = 0.1$ ° C/s, $G = 1000$ °C/m, and $n = 10^{11}$ pores/m^3 (note that for $\gamma_{lp} \to \infty$, n has almost no effect on the results). In Figure 10(a), the calculated final pore volume percentage (at steady state) is plotted as a function of the initial hydrogen content, C_0, for $P_{\sigma,\text{nuc}} = 0$, 1.6, and 16 bar. For $P_{\sigma,\text{nuc}} = 0$, ε_p increases almost linearly with increasing C_0. In contrast, at a given gas level, the porosity levels are significantly lower for the two nonzero values of $P_{\sigma,\text{nuc}}$. Interestingly, the predicted variations of ε_p with C_0 are quite similar for $P_{\sigma,\text{nuc}} = 1.6$ and 16 bar, except that a more pronounced "threshold" hydrogen level of $C_0 \approx 0.08$ $cc_{STP}H_2/100$ g Al, below which $\varepsilon_p \approx 0$, can be observed for $P_{\sigma,\text{nuc}} = 16$ bar. The similarity in the results for $P_{\sigma,\text{nuc}} = 1.6$ and 16 bar indicates that, for reasonably large $P_{\sigma,\text{nuc}}$ (and C_0 well above the threshold hydrogen level), the capillarity effect ceases to have an important influence on the final porosity levels. Note that $P_{\sigma,\text{nuc}} = 1.6$ bar is a physically reasonable value, whereas 16 bar is much too high. Finally, note the small but finite values of porosity seen in Figure 10(a) for low values of C_0. This porosity is shrinkage porosity that remains when the hydrogen level approaches zero. As seen in Figure 10(b), it does not form until solidification is almost complete (solid fraction above 95 pct). It could be argued that the remaining shrinkage porosity should be larger due to the presence of encapsulated liquid pockets at high solid fractions. However, Fang and Granger[14] measured porosity values less than 0.05 pct for low hydrogen levels, indicating that the encapsulated liquid pocket effect cannot be important. Even though the present permeability model does not completely cut off the feeding flow (*via* zero permeability) until the melt is completely solidified, the pressure reaches low enough values for some shrinkage porosity to form.

The predicted values of the solid fraction at which porosity first forms are plotted as a function of C_0 in Figure 10(b), for $P_{\sigma,\text{nuc}} = 0$, 1.6, and 16 bar. For $C_0 \to 0$, porosity starts to form at solid fractions close to unity, indicating as before that for $\dot{T} = 0.1$ ° C/s and $G = 1000$°C/m, the shrinkage contribution to porosity is negligibly small. With increasing initial hydrogen content, the solid fraction at which porosity first forms decreases strongly. In fact, for relatively large initial hydrogen contents (with the more reasonable value of $P_{\sigma,\text{nuc}} = 1.6$ bar), porosity can evolve at low solid fractions (*e.g.*, 30 pct), well before any eutectic starts to form. At a given initial hydrogen content, the solid fraction at which porosity first forms increases strongly with increasing $P_{\sigma,\text{nuc}}$. In other words, the higher the maximum capillary pressure, the later during solidification that porosity starts to form.

The effect of $P_{\sigma,\text{nuc}}$ on the predicted pore volume percentage is explored in greater detail in Figure 10(c), for $C_0 = 0.13$ $cc_{STP}H_2/100$ g Al. It can be seen that ε_p first decreases steeply as $P_{\sigma,\text{nuc}}$ increases from zero. For $P_{\sigma,\text{nuc}}$ greater than about 1 bar, on the other hand, ε_p is almost independent of $P_{\sigma,\text{nuc}}$. This enforces the observation in Figure 10(a) that, for reasonably large $P_{\sigma,\text{nuc}}$ (and C_0 well above the threshold hydrogen level), the capillarity effect ceases to have an important influence on the final porosity levels. Based on these results, the remainder of the simulations run for this study were performed with $P_{\sigma,\text{nuc}} = 1.6$ bar.

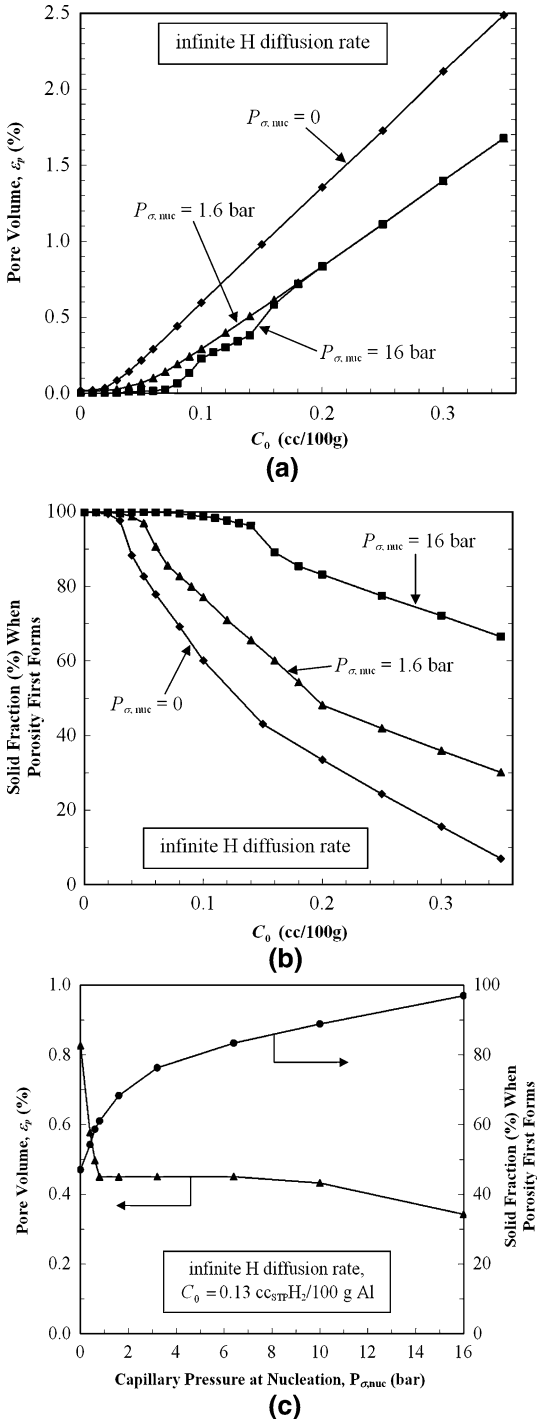

Fig. 10—Predicted steady-state results for infinitely fast local diffusion of hydrogen in the melt ($\gamma_{lp} \to \infty$): (*a*) variation of pore volume with C_0, (*b*) variation of solid fraction at pore formation with C_0, (*c*) variation of pore volume and solid fraction at pore formation with $P_{\sigma,\text{nuc}}$.

In order to better understand the effect of the cooling rate and the temperature gradient on the final pore

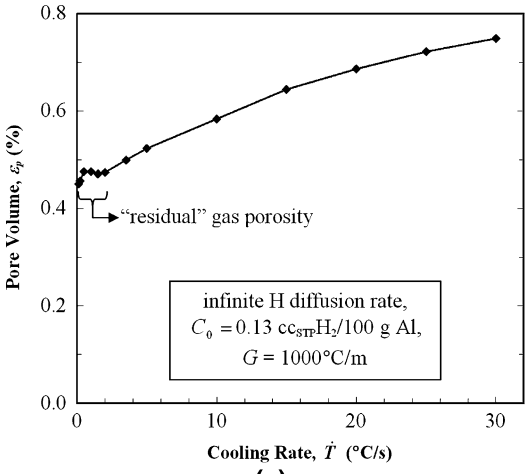

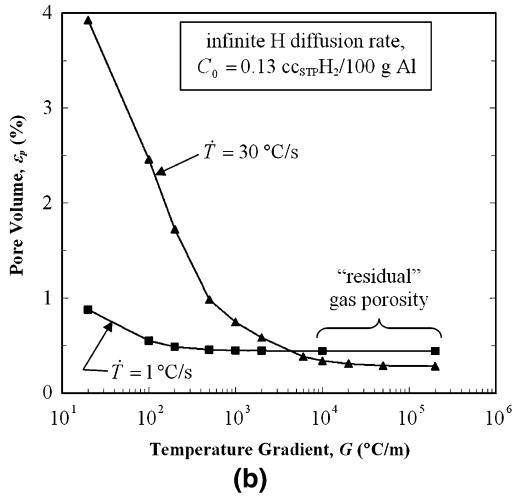

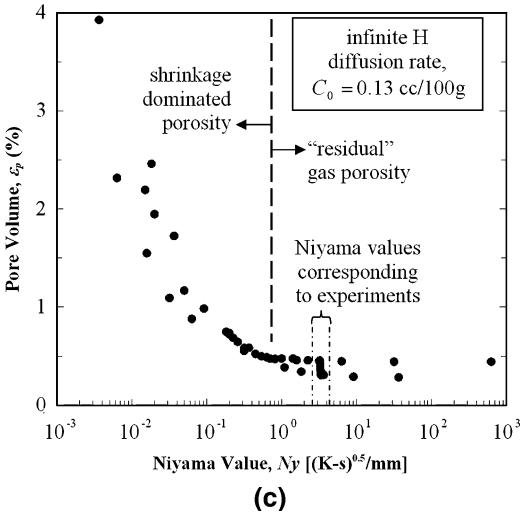

Fig. 11—Variation in pore volume percentage with (*a*) cooling rate, (*b*) temperature gradient, and (*c*) Niyama value, for simulations with infinite-rate hydrogen diffusion.

volume percentage, another parametric study was performed with infinitely fast local hydrogen diffusion in the melt (*i.e.*, $\gamma_{lp} \to \infty$), using $C_0 = 0.13$ cc/100 g and $n = 10^{11}$ pores/m^3. The results of this study are given in Figure 11. The effects of the cooling rate on pore volume, for $G = 1000$ °C/m, are shown in Figure 11(a). Once the cooling rate is larger than about 2 °C/s, a steady rise in pore volume is seen as the cooling rate increases. This is reasonable, because as the cooling rate rises, the dendrite arm spacing (SDAS) decreases, and thus the permeability decreases. A lower permeability provides more resistance to the feeding flow, which creates a larger pressure drop across the mushy zone that facilitates an increase in shrinkage porosity. Also, higher cooling rates imply shorter solidification times, which lead to higher feeding flow velocities and larger melt pressure drops. This is the same effect that was discussed in Section I, in connection with the Niyama criterion. The region below about 2 °C/s, marked "residual" gas porosity, shows porosity that is due simply to the level of hydrogen present in the solidifying melt. In this regime, the pore volume is almost independent of the cooling rate, and the feeding flow effects are not important.

The predicted pore volume percentage is shown as a function of temperature gradient in Figure 11(b). Above a certain value, the temperature gradient has little effect on the pore volume. However, for small temperature gradients (below about 200 °C/m for $\dot{T} = 1$°C/s and below about 6000 °C/m for $\dot{T} = 30$°C/s), it is evident that decreasing the temperature gradient causes an increase in the pore volume. This effect becomes magnified as the cooling rate increases. The increase in pore volume with decreasing temperature gradient is due to the increase in the size of the mushy zone as the gradient decreases. A larger mushy zone causes a larger pressure drop for the feeding flow. More difficulty in feeding leads to more shrinkage porosity. This observation is again in agreement with the Niyama criterion, because $Ny = G/\sqrt{\dot{T}}$, and the porosity increases as Ny decreases. At the higher temperature gradients, Figure 11(b) shows a region marked "residual" gas porosity, indicating a baseline level of gas porosity that is due to the hydrogen content in the melt rather than shrinkage. In other words, feeding flow effects are not important at large temperature gradients.

The results shown in Figures 11(a) and (b) are coupled in Figure 11(c), by combining the cooling rate and the temperature gradient using the Niyama criterion, $Ny = G/\sqrt{\dot{T}}$. It can be seen that all of the porosity predictions (for a given hydrogen level in the melt of $C_0 = 0.13$ cc/100 g), covering a wide range of cooling rates and temperature gradients, approximately collapse along a single line when plotted against the Niyama value. It is clear from Figure 11(c) that, below a Niyama value of about 0.7 (K s)$^{0.5}$/mm, the pore volume increases noticeably as the Niyama value decreases. This indicates the realm of shrinkage-dominated porosity. Above this value, however, there is a relatively constant value of porosity for all larger Niyama values. In this realm, shrinkage porosity is clearly not important and only residual gas porosity results. In summary, the Niyama criterion is indeed useful in predicting shrinkage porosity, but it cannot be used to predict gas porosity. It should be kept in mind that all results in Figure 11 are for a fixed hydrogen level in the melt and an infinite local hydrogen diffusion rate in the melt (*i.e.*, $\gamma_{lp} \to \infty$).

Finally, notice in Figure 11(c) the Niyama values corresponding to the experiments of References 13 and 14. These values, being between 3 and 4 $(K\ s)^{0.5}/mm$, are clearly not in the shrinkage-dominated regime. Thus, the experiments correspond to gas porosity only, as already mentioned in Section I. Figure 11 shows that for the case of infinitely fast local diffusion of hydrogen in the melt, gas porosity should not be strongly dependent on the temperature gradient or cooling rate.

A first attempt to compare measured and predicted porosities is shown in Figure 12. For the calculated pore volume percentages (filled symbols connected with lines), the temperature gradient at each cooling rate was taken from the function established earlier in this section to approximate the thermal conditions in the experiments (*i.e.*, $G = 3265\dot{T}^{0.512}$ °C/m). In this first attempt, the simulations were still performed for the limiting case of infinitely fast local hydrogen diffusion in the melt (*i.e.*, $\gamma_{lp} \to \infty$), using $n = 10^{11}$ pores/m^3. An initial hydrogen content of $C_0 = 0.13$ $cc_{STP}H_2$/100 g Al was used in Figure 12(a), while 0.26 $cc_{STP}H_2$/100 g Al was used in Figure 12(b). As expected from the results in Figure 11, the predicted porosities in Figure 12 are relatively independent of the cooling rate and, indirectly, of the temperature gradient, because they all correspond to the gas porosity regime. The slight decrease in pore volume with increasing cooling rate can be attributed to the corresponding decrease in dendrite arm spacing with increasing cooling rate. According to the present model, a smaller dendrite arm spacing reduces the pore radius and, hence, increases the capillary pressure. A higher capillary pressure generally results in less porosity. However, this effect is relatively weak, and the predicted decrease in the porosity with increasing cooling rate is not nearly strong enough to agree with the trend in the experimental data (open symbols).

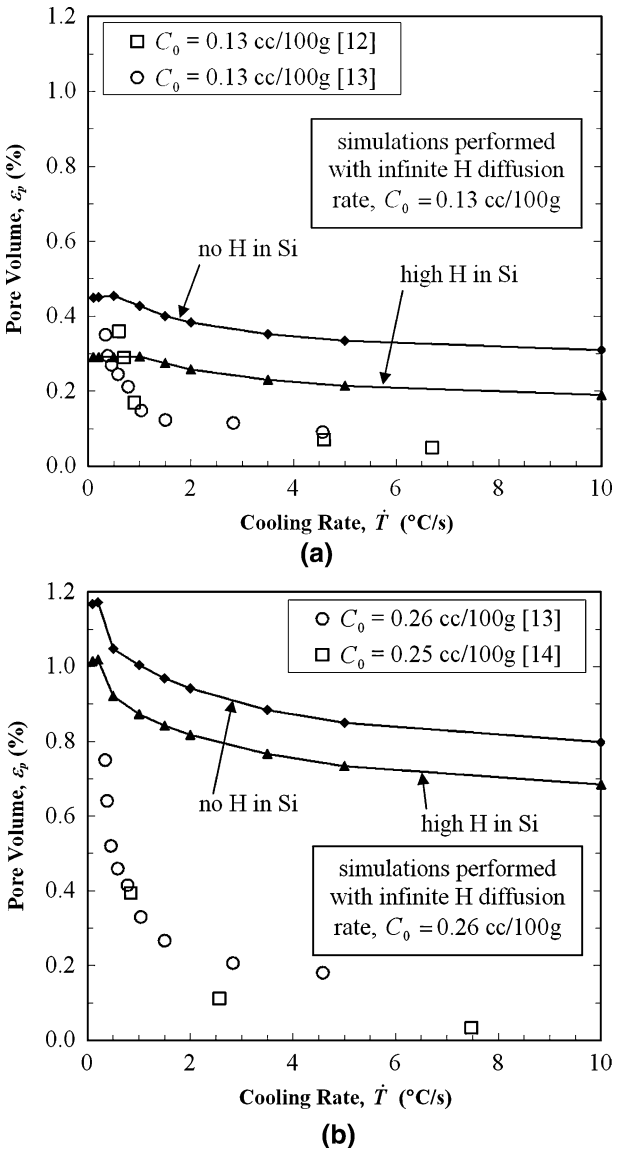

Fig. 12—Simulations with initial hydrogen concentrations of (*a*) 0.13 cc/100 g and (*b*) 0.26 cc/100 g. All simulations use an infinite hydrogen diffusion rate, a temperature gradient $G = 3265\dot{T}^{0.512}$ (°C/m), a pore density $n = 10^{11}$ m^{-3}, and a capillary pressure at nucleation of 1.6 bar. Experimental results[12,13,14] are shown for comparison.

Two sets of simulation results are shown in Figure 12: one set using the hydrogen partition coefficient based on the solid solubility given by Eq. [13] (labeled "$\kappa_{\text{high H in Si}}$" in Figure 5(a)) and one set using the partition coefficient based on the solid solubility given by Eq. [14] (labeled "$\kappa_{\text{no H in Si}}$" in Figure 5(a)). It is evident in Figure 12 that the different solid solubilities used to compute the partition coefficients lead to an almost constant offset in the resulting pore volume percentages. The simulations run assuming no hydrogen solubility in eutectic silicon and all have about 0.1 to 0.15 pct more porosity than the analogous simulations run assuming hydrogen solubility in eutectic silicon based on the data in Reference 29. In considering which partition coefficient produces results most closely matching experimental values, the results in Figure 12 are somewhat inconclusive. Little information can be gained from Figure 12(b), because both simulation curves are above all experimental data. However, Figure 12(a) provides some insight because at low cooling rates, the predicted porosities with "high H in Si" are lower than the measured values. This indicates that $\kappa_{\text{high H in Si}}$ may not be appropriate to use. Including in the model finite-rate local diffusion of hydrogen in the melt would only lower the porosity predictions further (as subsequently discussed), and thus would not correct the predictions being below the measurements. Uncertainties in the permeability are also not an issue here, because the predictions in Figure 12 do not correspond to shrinkage porosity, as noted previously. The only remaining uncertainty in the model predictions is the choice of the pore density in Figure 12, *i.e.*, $n = 10^{11}$ pores/m^3. Therefore, the effect of the pore density is explored next.

Figure 13(a) shows three sets of simulation data corresponding to three different pore number densities: $n = 10^{10}$, 10^{11}, and 10^{12} pores/m^3. The results presented in Figure 13(a) are from simulations with $C_0 = 0.13$ cc/100 g, $\gamma_{lp} \to \infty$, $\kappa_{\text{no H in Si}}$, and $G = 3265\dot{T}^{0.512}$ °C/m. It can be seen that at high cooling rates, all three pore densities produce similar pore volumes. However, for lower cooling rates, there is significant variation between

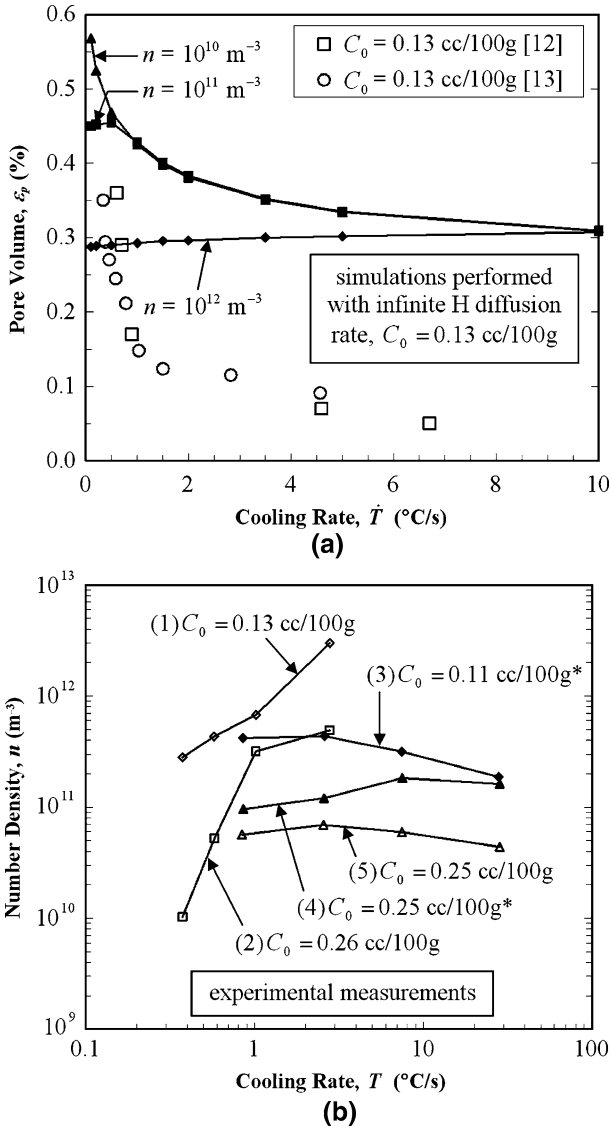

Fig. 13—(*a*) Simulated variation of pore volume with cooling rate, for three different pore number densities. (*b*) Experimentally measured number densities as a function of cooling rate with several initial hydrogen concentrations. Experimental data (1–2) are from Emadi and Gruzleski,[13] while (3–5) are from Fang and Granger.[14] Values with asterisks (3, 4) are grain refined; all data are unmodified A356.

these results. The results for 10^{12} pores/m^3 are independent of cooling rate. However, the results for 10^{11} pores/m^3 show an increase as the cooling rate decreases. The results for 10^{10} pores/m^3 are similar to those for 10^{11} pores/m^3 down to about 0.5 °C/s, with higher pore volume percentages for cooling rates below this level. These differences can again be attributed to capillary pressure variations. For 10^{10} and 10^{11} pores/m^3, the pore radius is primarily controlled by the dendrite arm spacing, which decreases with increasing cooling rate; smaller pore radii result in larger capillary pressures and less pore volume, as already explained in connection with Figure 12. As the pore number density increases, the pore radius decreases (for a given pore volume) until it is no longer controlled by the dendrite arm spacing and is simply given by r_{sphere} (Eq. [11]). This can be observed for 10^{12} pores/m^3: the dendrite arm spacing has no effect on the pore radius or the capillary pressure, and the predicted porosity becomes virtually independent of the cooling rate. Recall that the simulations in this figure are still for the limiting case of infinitely fast local diffusion of hydrogen in the melt. Figure 13(b) shows pore number densities obtained from experimental results for unmodified A356.[13,14] These densities were derived using the pore volume percentages and average pore diameters reported in References 13 and 14, assuming spherical pores and determining the number density from the relation $n = 6\varepsilon_p/\pi d^3$, where ε_p is the pore fraction and d is the average pore diameter. As seen in Figure 13(b), there is a large variation in the pore number densities derived in this manner, with few apparent trends in the data. The pore number densities range from about 10^{10} to 10^{12} pores/m^3, and 10^{11} pores/m^3 can be regarded as a reasonable mean value. Note that the pore number densities for the lower hydrogen levels are all above 10^{11} pores/m^3. Considering this fact in conjunction with the results in Figure 13(a), it is unlikely that any uncertainty in the pore number density would cause an upward shift of the curve in Figure 12(a) labeled "high H in Si". Based on this very limited evidence, the hydrogen partition coefficient $\kappa_{\text{high H in Si}}$ is no longer considered in the present study.

Finally, the effect of finite-rate diffusion of hydrogen in the liquid on pore formation, as modeled by Eq. [8], is investigated in Figures 14 and 15. The simulation results in these figures were generated using $G = 3265\dot{T}^{-0.512}$ °C/m, $n = 10^{11}$ pores/m^3, $P_{\sigma,\text{nuc}} = 1.6$ bar, and assuming no hydrogen solubility in the eutectic silicon. In both Figures 14 and 15, the analogous simulation results with $\gamma_{lp} \to \infty$ are included for reference (labeled "infinite H diffusion rate").

Figure 14 investigates the effect that the impingement factor, $\phi = (1-\varepsilon_s)^m$, has on the predicted final pore volume percentages. Recall that the impingement factor

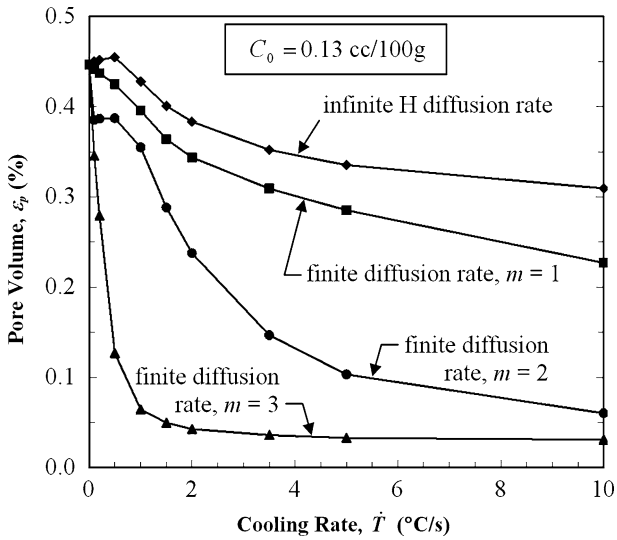

Fig. 14—Simulations demonstrating the effect of the impingement factor ($\phi = (1-\varepsilon_s)^m$) on final pore volume percentages. All results shown use a temperature gradient $G = 3265\dot{T}^{-0.512}$ (°C/m), a pore density $n = 10^{11}$ m^{-3}, and a capillary pressure at nucleation of 1.6 bar.

is used to determine the pore-liquid interfacial area concentration, S_{lp}, in the finite-rate hydrogen diffusion equation (Eq. [8]) and that Figure 3 illustrates how the impingement factor varies for different values of the exponent m. Final pore volume results are given in Figure 14 for finite-rate hydrogen diffusion simulations with three different values of m, along with the analogous simulation results for infinite-rate diffusion. Notice that the porosity results change dramatically as the value of m changes. The pore volumes for finite-rate hydrogen diffusion with $m = 1$ are only slightly lower than for infinite-rate diffusion. The difference grows slowly as the cooling rate increases, because less time is available for diffusion at higher cooling rates. The effect of finite-rate diffusion becomes more pronounced for $m = 2$, with the pore volume dropping significantly below infinite-rate values for cooling rates above about 1 °C/s. The results for $m = 3$ show a dramatic difference between finite-rate and infinite-rate diffusion. For cooling rates less than about 1 °C/s, the pore volume percentages for $m = 3$ decrease sharply with increasing cooling rate. Above about 1 °C/s, the pore volume begins to level off, reaching a nearly constant value of about 0.03 pct at about 4 °C/s. Notice that, in the limit of zero cooling rate, the finite-rate results for all values of m approach the infinite-rate value of 0.45 pct. As the cooling rate approaches zero, the solidification time becomes very large, and ample time is available for hydrogen to fully diffuse from the liquid to the pores. It is interesting to note the different nature of the curves for $m = 1$, 2, and 3 as the cooling rate approaches zero: for $m = 3$, the limiting value for the zero cooling rate is approached almost asymptotically, while for $m = 2$, a small plateau is reached at about 0.5 °C/s, and the pore volume does not begin to approach the limiting value until the cooling rate is below 0.1 °C/s.

Figure 15 compares experimentally measured pore volume percentages with those from simulations using both infinite-rate and finite-rate ($m = 3$) hydrogen diffusion. In Figure 15(a), the initial hydrogen content is fixed at $C_0 = 0.13$ cc/100 g, while in Figure 15(b), the content is $C_0 = 0.26$ cc/100 g. It can be seen that the pore volumes resulting from the finite-rate diffusion simulations show a steep decrease in pore volume with increasing cooling rate similar to that seen in the experimental results, unlike the infinite-rate diffusion results. The parametric studies presented earlier in this section indicate that no other physical mechanism can be responsible for this steep decrease in porosity; hence, it can only be explained by the reduction in the pore growth rate due to finite-rate diffusion of hydrogen in the melt. Note that the finite-rate diffusion predictions, shown in Figure 15 for $m = 3$, somewhat underpredict the pore volumes for $C_0 = 0.13$ cc/100 g and somewhat overpredict the pore volumes for $C_0 = 0.26$ cc/100 g. Thus, other values for m would not produce better overall agreement. This remaining disagreement between the measurements and predictions could be the result of the present model for the impingement factor being too simple or of uncertainties in other aspects of the model or the input data. For example, as shown in Figure 13(b), it is possible that the number density of

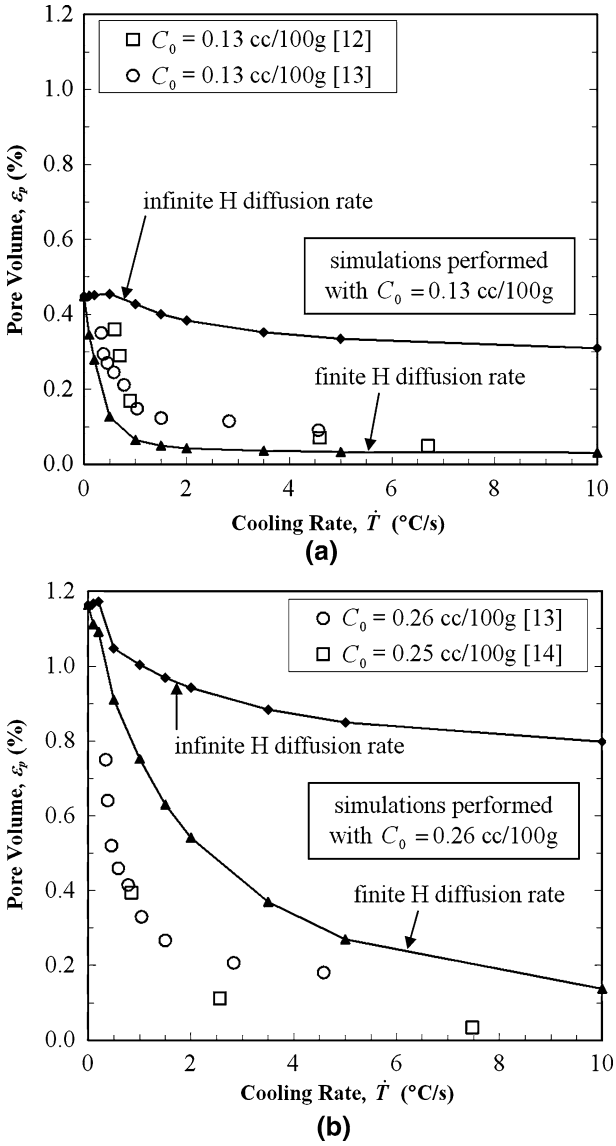

Fig. 15—Simulations with initial hydrogen concentrations of (*a*) 0.13 cc/100 g and (*b*) 0.26 cc/100 g, with both finite and infinite hydrogen diffusion rates. Results shown use a temperature gradient $G = 3265\dot{T}^{-0.512}$ (°C/m), a pore density $n = 10^{11}$ m^{-3}, and a capillary pressure at nucleation of 1.6 bar. Experimental results[12,13,14] are shown for comparison.

pores, n, varies with the initial hydrogen content or the cooling rate; such a variation could easily be responsible for the remaining disagreement in Figure 15. The lack of more complete experimental data prevents a more definitive exploration of this effect. Despite these uncertainties, Figure 15 does clearly indicate the importance of finite-rate hydrogen diffusion in gas porosity formation in aluminum alloys.

V. CONCLUSIONS

A volume-averaged model has been developed for predicting shrinkage and gas porosity formation during solidification of aluminum alloys. The model accounts not only for the effects of feeding flow and melt pressure

variations, but also for the local, finite-rate diffusion of dissolved hydrogen in the liquid toward the pores. Numerous parametric studies are presented that explore the effects of the capillary pressure at pore nucleation, the applied cooling rate and temperature gradient, the solubility of hydrogen in the eutectic solid, the pore number density, and the pore-solid interface impingement factor. It is shown that shrinkage driven porosity becomes important for high cooling rates and low-temperature gradients, when $Ny = G/\sqrt{\dot{T}} < 0.7$ (K s)$^{0.5}$/mm. In the gas porosity regime, comparisons with previous experimental measurements show that pore growth can indeed be limited by finite-rate diffusion of hydrogen. Overall, good agreement is obtained between predicted and previously measured pore volumes in directionally solidified, unmodified A356 alloys. In particular, it is shown that the observed strong decrease in the porosity with increasing cooling rate can only be explained by the finite-rate diffusion effect. Additional work is needed to (1) more accurately measure the solubility of hydrogen in the eutectic solid, (2) incorporate a more realistic model for the pore number density variations, and (3) further improve the accuracy of the local, finite-rate hydrogen diffusion submodel (*e.g.*, the impingement factor). It would also be of interest to validate the present model for grain-refined or modified aluminum alloys, as well as for aluminum alloys of a different composition. Although the present study focused on directional solidification with a prescribed temperature variation, it is straightforward to extend the model to cases where the temperature must be calculated. Due to its volume-averaged nature, the model can readily be used in conjunction with fully three-dimensional casting simulations.

ACKNOWLEDGMENTS

This work was supported, in part, by the United States National Science Foundation under Grant No. DMR-0132225 and by Magma Foundry Technologies.

REFERENCES

1. T.S. Piwonka and M.C. Flemings: *Trans. AIME*, 1966, vol. 236, pp. 1157–65.
2. K. Kubo and R.D. Pehlke: *Metall. Trans. B*, 1985, vol. 16B, pp. 359–66.
3. P.D. Lee, A. Chirazi, and D. See: *J. Light Met.*, 2001, vol. 1, pp. 15–30.
4. A.S. Sabau and S. Viswanathan: *Metall. Mater. Trans. B*, 2002, vol. 33B, pp. 243–55.
5. C. Pequet, M. Gremaud, and M. Rappaz: *Metall. Mater. Trans. A*, 2002, vol. 33A, pp. 2095–2106.
6. P.D. Lee and J.D. Hunt: in *Modeling of Casting, Welding and Advanced Solidification Processes VII*, M. Cross and J. Campbell, eds.(TMS, Warrendale, PA, 1995), pp. 585–92.
7. P.D. Lee, and J.D. Hunt: *Acta Mater.*, 1997, vol. 45, pp. 4155–69.
8. R.C. Atwood, S. Sridhar, W. Zhang, and P.D. Lee: *Acta Mater.*, 2000, vol. 48, pp. 405–17.
9. R.C. Atwood and P.D. Lee: *Metall. Mater. Trans. B*, 2002, vol. 33B, pp. 209–21.
10. R.W. Hamilton, D. See, S. Butler, and P.D. Lee: *Mater. Sci. Eng. A*, 2003, vol. A343, pp. 290–300.
11. K. Tynelius, J.F. Major, and D. Apelian: *AFS Trans.*, 1993, vol. 101, pp. 401–13.
12. R. Fuoco, H. Goldenstein, and J.E. Gruzleski: *AFS Trans.*, 1994, vol. 102, pp. 297–306.
13. D. Emadi and J.E. Gruzleski: *AFS Trans.*, 1994, vol. 102, pp. 307–11.
14. Q.T. Fang and D.A. Granger: *AFS Trans.*, 1989, vol. 97, pp. 989–1000.
15. E. Underwood: *Quantitative Stereology* (Addison-Wesley Publishing CoReading, MA, 1970), pp. 27, 96, and 103.
16. E. Niyama, T. Uchida, M. Morikawa, and S. Saito: *Am. Foundrymen's Soc. Int. Cast Met. J.*, 1982, vol. 7(3), pp. 52–63.
17. K.D. Carlson, S. Ou, R.A. Hardin, and C. Beckermann: *Metall. Mater. Trans. B*, 2002, vol. 33B, pp. 731–40.
18. K.D. Carlson, Z. Lin, R.A. Hardin, C. Beckermann, G. Mazurkevich, M.C. Schneider: in D.M. Stefanesu, J.A. Warren, M.R. Jolly, and M.J.M. Krane, eds., *Modeling of Casting, Welding and Advanced Solidification Processes X*, TMS, Warrendale, PA, 2003, pp. 295–302.
19. S. Shivkumar, D. Apelian, and J. Zou: *AFS Trans.*, 1990, vol. 98, pp. 897–904.
20. J.D. Zhu, S.L. Cockcroft, D.M. Maijer, and R. Ding: *Int. J. Cast Met. Res.*, 2005, vol. 18 (4), pp. 229–35.
21. D. Emadi, J.E. Gruzleski, and J.M. Toguri: *Metall. Trans. B*, 1993, vol. 24B, pp. 1055–63.
22. M.J. Moran and H.N. Shapiro: *Fundamentals of Engineering Thermodynamics* (John Wiley & SonsInc, New York, NY, 2004), pp. 102 and 759.
23. W. Eichenauer and J. Markopoulos: *Z. Metallkd.*, 1974, vol. 65 (10), pp. 649–52.
24. P.N. Anyalebechi: *Scripta Metall. Mater.*, 1995, vol. 33 (8), pp. 1209–26.
25. J. Ni and C. Beckermann: *Metall. Trans. B*, 1991, vol. 22B, pp. 349–61.
26. *JMatPro*, Sente Software Ltd., Surrey Technology Centre, Surrey GU2 7YG, United Kingdom.
27. S. Thompson, S.L. Cockcroft, and M.A. Wells: *Mater. Sci. Technol.*, 2004, vol. 20, pp. 194–200.
28. D.R. Poirier and P.K. Sung: *Metall. Mater. Trans. A*, 2002, vol. 33A, pp. 3874–76.
29. M. Ichimura and Y. Sasajima: *J. Jpn. Inst. Light Met.*, 1993, vol. 43(7), pp. 385–91.
30. P.N. Anyalebechi: in B. Welch, ed., *Light Metals 1998*, TMS, Warrendale, PA, 1998, pp. 827–42.
31. R.C. Newman: *J. Phys.: Condens. Matter*, 2000, vol. 12, pp. R335–R365.
32. MAGMASOFT, MAGMA GmbH, 52072 Aachen, Germany.